The Role of Pore Geometry in Single Nanoparticle Detection

Matthew Davenport,[†,‡] Ken Healy,[‡,§] Matthew Pevarnik,[‡] Nick Teslich,[†] Stefano Cabrini,[⊥] Alan P. Morrison,[§] Zuzanna S. Siwy,[‡] and Sonia E. Létant[†,*]

[†]Physical and Life Sciences, Lawrence Livermore National Laboratory, 7000 East Avenue, Livermore, California 94550, United States, [‡]Department of Physics and Astronomy, University of California, Irvine, 4129H Frederick Reines Hall Irvine, California 92697-4575, United States, [§]Department of Electrical and Electronic Engineering, University College, Cork, Ireland, and [⊥]Molecular Foundry, Lawrence Berkeley National Laboratory, 1 Cyclotron Road, Berkeley, California 94720, United States

ABSTRACT We observe single nanoparticle translocation events *via* resistive pulse sensing using silicon nitride pores described by a range of lengths and diameters. Pores are prepared by focused ion beam milling in 50 nm-, 100 nm-, and 500 nm-thick silicon nitride membranes with diameters fabricated to accommodate spherical silica nanoparticles with sizes chosen to mimic that of virus particles. In this manner, we are able to characterize the role of pore geometry in three key components of the detection scheme, namely, event magnitude, event duration, and event frequency. We find that the electric field created by the applied voltage and the pore's geometry is a critical factor. We develop approximations to describe this field, which are verified with computer simulations, and interactions between particles and this field. In so doing, we formulate what we believe to be the first approximation for the magnitude of ionic current blockage that explicitly addresses the invariance of access resistance of solid-state pores during particle translocation. These approximations also provide a suitable foundation for estimating the zeta potential of the particles and/or pore surface when studied in conjunction with event durations. We also verify that translocation achieved by electro-osmotic transport is an effective means of slowing translocation velocities of highly charged particles without compromising particle capture rate as compared to more traditional approaches based on electrophoretic transport.

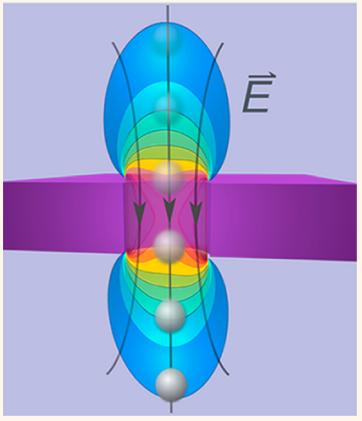

KEYWORDS: nanopore · nanoparticle · resistive-pulse · aspect ratio · ion current

Single particle detection techniques based on driving nanoparticles through submicrometer or nanoscopic pores with a voltage or pressure gradient have been the subject of numerous studies over the past two decades.[1] This, in large part, is due to the potential of nanopore-based platforms to differentiate between base pairs of nucleic acid chains as the molecule threads through the pore, which could provide a low-cost, high-throughput means of DNA sequencing.[2−10] However, the history of pore-based detection schemes starts much earlier, nearly 60 years ago, with the counting of blood cells as they passed through a microscopic hole in a glass tube.[11] Based on the same principles, these recent strides toward DNA sequencing are a result of key advancements in the interim.

In the context of solid-state nanopores, the key advancements were technological in nature; micro- and nanofabrication techniques were developed to allow for the production of smaller holes to address smaller and more fundamental biological particles, such as the aforementioned DNA, but also including RNA and proteins.[6,12,13] Between microscopic cells and their nanoscopic building blocks, however, exist a class of particles as important biologically as they are to the development of pore-based particle detection: viruses, which range from roughly 20 nm to upward of 600 nm. Scale is perhaps the most important consideration in the pore sensing technique. Ions from the background electrolyte are temporarily excluded from the pore as the particle moves through it, or translocates, transiently reducing the ionic current as shown in Scheme 1. The magnitude of this change in current, or event, along with its duration provides information regarding the particle's size and surface chemistry. Conversely, if the particle is well characterized in terms of size and chemistry, one can study how variations in the pore's properties influence particle translocation and the transduction thereof.[14,15] In this report, we focus on the theme of scale to investigate how a pore's length and diameter affect the shape of the event, along with the nature of the transport mechanisms that drive translocation.

Studies conducted over the past several years provide a wealth of information on this front, but the data tends to accumulate in one of two extremes which can be

* Address correspondence to letant1@llnl.gov.

Received for review July 12, 2012 and accepted August 22, 2012.

Published online August 22, 2012
10.1021/nn303126n

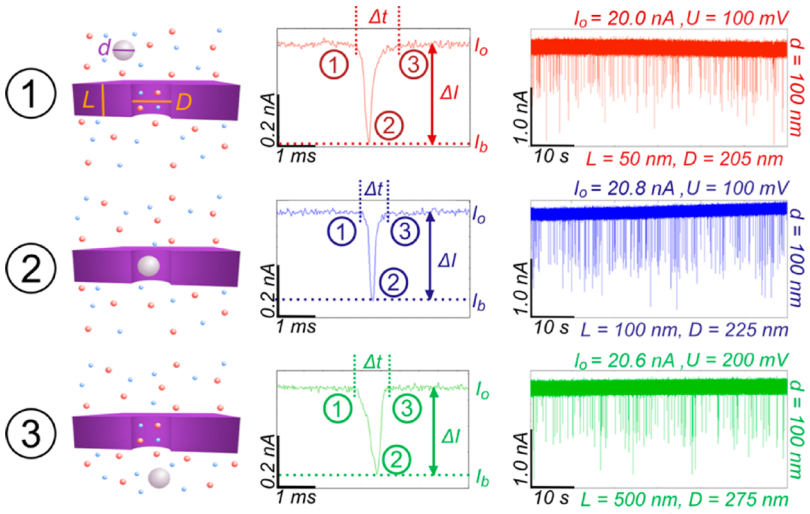

Scheme 1. As a particle of diameter *d* approaches a pore, described by its own diameter *D* and length *L*, the current begins to drop from its baseline, open value, I_o (1), to a blocked value, I_b (2). The magnitude of the difference between these levels, ΔI, is recorded along with the duration of the translocation events—that is the time it takes for the particle to pass through the pore and the current to return to I_o (3). Several hundred such events are collected during a typical scan so that distributions for both event magnitudes and durations can be statistically analyzed. The scale bar for ionic current is included to indicate depths of events rather than the magnitude of the open pore currents, which are all ~20 nA for the experiments shown. While the role of the transmembrane electric potential difference, *U*, is not explicitly shown in this figure, it can be understood to be the source of the force which drives particles and ions through the pore for the purposes of this figure.

understood in terms of the pore aspect ratio, that is its length divided by its diameter. Early (*circa* 1970) studies focused on high aspect ratio pores, which could be considered long and narrow with lengths orders of magnitude larger than the particle being detected.[14,16,17] That is not to say that more recent publications do not also use these types of pores, but more modern fabrication techniques are allowing for smaller pore diameters and even higher aspect ratios, which are able to more intimately probe particles.[18−24] These glass and polymeric pore materials present a set of challenges: there is no straightforward manner in which to reduce the thickness of the membrane, and thus pore length, to less than ~1 μm or in which to integrate these nanopores into microelectromechanical systems (MEMS) to enable high-throughput, small volume lab-on-a-chip-type device architectures. These challenges have lead researchers to probe different materials and a new extreme.

Silicon nitride pores are amenable to a wide range of fabrication techniques—the choice is generally guided by the size of the target analyte—and are easily integrated with commonly used microfluidic systems. Silicon nitride membranes can be deposited in a wide range of thicknesses, from nanometer to micrometer, which has allowed researchers to investigate virion-sized particles with low to ultralow aspect ratio pores.[25−27] There are studies in the intermediate aspect ratio regime utilizing other solid-state devices, but these examine single pore geometries and tend to rely on the same analysis as high aspect ratio pores.[28−32] For this reason, we wanted to examine a range of pore lengths and diameters to bridge these gaps in both data and understanding.

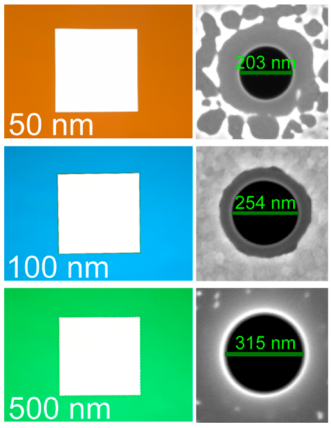

Figure 1. (Left) Optical microscope images of the free-standing silicon nitride membranes which appear as bright squares. The surrounding colored regions are caused by the thin-film interference of the nitride layer on the silicon support. (Right) SEM micrographs of nanopores representing the range of pore diameters studied: *ca.* 200−300 nm.

RESULTS AND DISCUSSION

To build upon the framework of earlier studies, we examine a range of silicon nitride membrane thicknesses (*L*) and pore diameters (*D*) as shown in Figure 1. A focused ion beam (FIB) is used to mill pores with diameters ranging from roughly 200 to 300 nm in 50, 100, and 500 nm-thick membranes. The membranes are easily identified by their colors which result from the thin film interference caused by the silicon nitride

layer on top of a silicon support frame: 50 nm membranes have a dark red hue, 100 nm membranes are blue, and 500 nm membranes appear green as shown in the optical microscope images in the left-hand column of Figure 1. This color scheme is employed throughout the text, meaning data presented in red correspond to L = 50 nm membranes and so forth. To test the response of a given combination of pore length and diameter to a range of particle sizes, silica nanoparticles defined by two distinct size distributions, with mean particle diameters (d) of 57 and 101 nm, were chosen to highlight a subset of virion sizes. Micrographs of the particles along with their size distributions can be found in Figure 2d (size distributions were obtained using SEM images along with ImageJ image analysis software).[33] For the purposes of this text, we will use the nominal diameters as supplied by the vendor for distinction, that is, 50 and 100 nm.

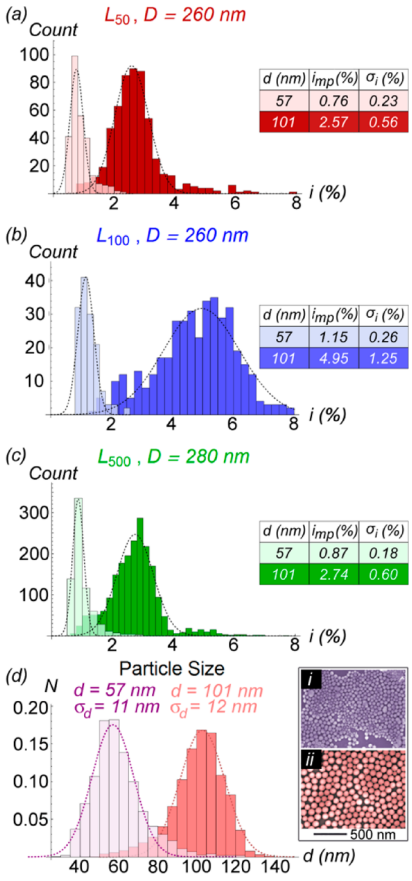

Figure 2. (a–c) Histograms showing event depth distributions for each membrane thickness. Gaussian PDF parameters gained from these experiments are expressed for each particle size. Note the similarities in shape between event depth and particle size distributions shown in panel d. Particles were measured using an SEM; representative micrographs for 50 and 100 nm beads are shown in insets (i) and (ii), respectively (micrographs are false colored to match histograms).

The rightmost column of Scheme 1 includes ionic current traces from experiments involving three different pore geometries with 100 nm particles. In these sixty second "clips" of the experiments (which typically last around 10 min), one can already see that a typical experiment contains several unique events, each of which is characterized by a depth and duration. By conducting several such experiments, we are able to construct a systematic study of the role of the geometry of a pore in its response to a translocating particle. In the context of resistive pulse sensing, this examination of response involves identifying the probability distribution functions, or PDFs, that best describe the distributions of event depths and event durations, extracting the parameters that define these distributions and assessing how these parameters vary with pore geometry, particle size, and applied voltage. Over the course of developing and discussing the significance of these PDFs in relation to these parameters, several variables will be introduced, so we present Table 1 as a quick reference guide for our notation.

TABLE 1. Variable Definitions

variable	definition	variable	definition	variable	definition
D	pore diameter	I_o	open ionic current	v_{mp}	most probable translocation velocity
L	pore length	I_b	blocked ionic current	r	radial distance from pore mouth
d	particle diameter	i	event depth; $(I_o - I_b)/I_o$	v_{EP}	electrophoretic velocity for $r \leq D$
U	applied electric potential difference	i_{mp}	most probable event depth	v_{EO}	electro-osmotic velocity for $r \leq D$
R	total pore resistance	Δt	event duration	v	particle velocity for $r > D$
R_p	geometric resistance	Δt_{mp}	most probable event duration	E_z	electric field for $r \leq D$
R_a	access resistance	τ	event duration time constant	E_{cis}	electric field for $r > D$
α	R_a/R_p	τ	time between events	ζ_{pore}	pore zeta potential
β	field interaction coefficient	f	event frequency	$\zeta_{particle}$	particle zeta potential
χ	pore volume excluded by particle	ξ	event frequency scaling factor	δ	diffusion coefficient

In the event that a variable is subscripted with a number, it is understood that the number indicates the dimension used to identify the object, for example, L_{50} = 50 nm long pore and d_{100} = 100 nm diameter particle. When zeta potentials and diffusion coefficients are subscripted with "d50" or "d100", it is understood to reference the value for 50 or 100 nm particles, respectively. For example, ζ_{d50} would be the zeta potential of 50 nm particles and δ_{d100} is the diffusion coefficient for 100 nm particles.

Event Depth. Depending on the report, event depths may be reported in terms of the magnitude of the change in pore resistance, R, from an unobstructed, open state to a blocked state (subscripted with an "o" or "b" respectively), $\Delta R = |R_o - R_b|$, or the change in ionic current, $\Delta I = |I_o - I_b|$. Of course, this blockage is caused by the translocating particle. Frequently, these quantities are presented relative to their values measured in the absence of particles, $\Delta R/R_o$ or $\Delta I/I_o$. Because our pores impede ionic current in an entirely ohmic fashion, resistance and current can be used interchangeably with the appropriate application of Ohm's law:

$$U = IR \tag{1}$$

where U is the applied electric potential difference across the membrane. Since I and U are continuously monitored by the patch-clamp amplifier during bead translocation, it is straightforward to evaluate the quantity of our choosing and we have found each to be useful in interpreting our results.

Understanding the pore resistance is crucial as it immediately relates a pore's geometry to the behavior of the system. Let R represent the sum of all the resistive elements impeding current. For our pores, R represents the sum of the series combination of the pore's geometric resistance, R_p, and its access resistance, R_a. Our pores are, to first order, cylindrical, allowing us to write

$$R_p = \frac{4L}{\pi\kappa D^2} \tag{2}$$

where κ is the conductivity of the electrolyte. The access resistance is a consequence of ions converging to a small aperture from a semi-infinite reservoir, a consideration which was explored over 40 years ago as researchers began to understand the function and conductance of pores embedded in biological membranes. As shown by Hall in 1975, this resistance is dependent upon just one component of the pore's geometry: its diameter.[34]

$$R_a = 2 \times \frac{1}{2\kappa D} = \frac{1}{\kappa D} \tag{3}$$

The factor of 2 comes from both the pore entrance and exit contributing to the overall access resistance. The total resistance is then given by summing eqs 2 and 3:

$$R = R_p + R_a = \frac{4L + \pi D}{\pi\kappa D^2} \tag{4}$$

giving the relationship between the current established by applying a voltage and pore geometry.

However, we chose to present our results primarily as $\Delta I/I_o$ to emphasize that, in every device, current is being measured and the division by the baseline current value allows for a more direct comparison of pores over the variables considered. To simplify notation, we introduce $i = \Delta I/I_o$ to indicate the event depth as a current relative to its baseline value, reported as a percentage. As the probability distribution associated with event depths is Gaussian, the relevant parameters are the most probable event depth, i_{mp}, and the variance, σ_i^2 (or simply σ_i, the standard deviation).

$$P(i) = C\, e^{-(i - i_{mp})^2/\sigma_i^2} \tag{5}$$

with C being a constant of normalization.

Figure 2 shows histograms and their corresponding Gaussian curves and fit parameters for three pores of similar diameters fabricated in silicon nitride films with thicknesses of (a) 50 nm, (b) 100 nm, and (c) 500 nm. For each, we observe large values of σ_i relative to the mean event depth values, which is easily understood considering the particle size distributions, again, shown in Figure 2d. Given that the i histograms also capture the shape of the particle size histograms—skewed slightly to higher values for the 50 nm particles and slightly toward lower values for the 100 nm particles—and that peaks are narrower for d_{50} particles versus d_{100} particles, we are confident that it is the variation in particle diameter that dictates the magnitude of σ_i for a given pore geometry. Therefore, we assume that inhomogeneities in the manner in which the particles translocate the pore do not influence the PDF's shape, for example, differences which could be attributed to particles that travel along the pore's central axis *versus* those that do not are negligible. In this light, larger σ_i values are favorable as they suggest a heightened sensitivity to particles of a different size; however, since the particle size distribution is continuous, the size resolution of the devices cannot be determined.

A quick comparison of the i_{mp} resulting from each histogram suggests that working with the shortest pore does not guarantee the largest relative change in current. In the context of the previous discussion of the resistive pulse mechanism, which is based on the particle excluding current carrying ions from the pore's volume during translocation, this result is somewhat surprising: for a given ratio of particle diameter to pore diameter, decreasing the pore length decreases the fraction of the pore's volume occupied by current carrying ions, which would seemingly result in greater values of i_{mp}. As one set of histograms does not constitute a trend, we present all the values of i_{mp} over the range of pore geometries studied in Figure 3a–c).

To more conclusively demonstrate that excluded volume alone does not sufficiently quantify event depths, the most probable i values are first plotted as unfilled markers against χ, the ratio of the pore's volume occupied by a particle to the total pore volume:

$$\chi = \begin{cases} \dfrac{2d^2}{3D^2}, d > L \\ \dfrac{2d^3}{3LD^2}, d \le L \end{cases} \tag{6}$$

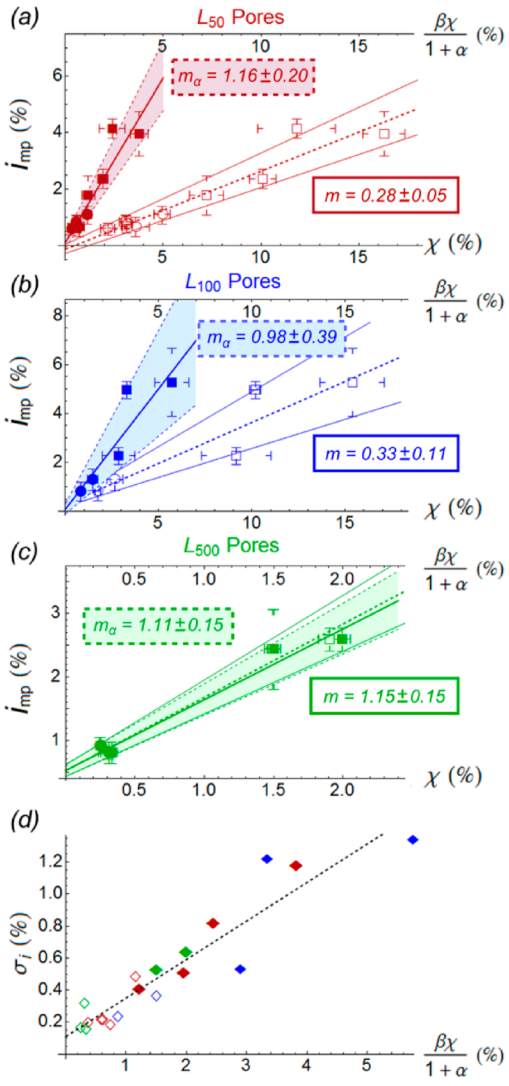

Figure 3. (a−c) Most probable *i* values are plotted for each membrane thickness versus the excluded volume, χ (empty markers), and $\beta\chi/(1+\alpha)$ (filled markers). Circles represent data collected for d_{50} particles and d_{100} experiments are shown as squares. Best fit lines are plotted for each case and bounded by lines accounting for uncertainties in the slope value. For excluded volume alone, the best fit line is dashed and with solid bounding lines. The area between these bounds is white. For $\beta\chi/(1+\alpha)$, the best fit line is solid and the bounding lines are dashed with the area between filled with the color corresponding to the membrane thickness. Abscissa values are determined by averaging SEM and electrochemical sizing of *D*; the error bars are a reflection of the uncertainty in *D*. (d) Standard deviation versus $\beta\chi/(1+\alpha)$ is also found to be linear, supporting both the idea that our model is an improvement to event depth prediction and that the large standard deviations are related to the broad range of particle sizes. Empty diamonds represent d_{50} results and filled points are shown for d_{100}.

Note that these plots appear linear, which implies that the event depth is certainly and intimately tied to the excluded volume and also supports the recent report that this simple consideration alone can be useful for approximating i_{mp} in 50 nm membranes.[26] Each scatter has been fit according to $i_{mp} = m\chi + b$. The intercept, *b*, should be 0: a χ of 0 simply means there is no particle in the pore and there should be no change in current. An inspection of the plots reveals that, for 50 and 100 nm membranes, the expected value is well within experimental uncertainty, but is larger for 500 nm membranes. Given the fabrication method, we expect a gentle taper in the pores, resulting in a slight reduction in their diameter along their length. This reduction would then be most significant in thicker membranes. Because of this, we have likely underestimated χ in the 500 nm membranes resulting in a $b > 0$. Variations in the slope values, *m*, are more telling as they are related to the event depths functional dependence on the pore's geometry (rather than a systematic offset). Note the range of values from $m \approx 0.3$ in L_{50} and L_{100} pores to nearly 1.0 in L_{500} pores. A slope of 1 in this case would suggest that the current depth can be well-characterized by the excluded volume alone. While sufficient for 500 nm long pores, this consideration is clearly lacking important elements especially relevant in thinner membranes.

While there exist rigorous theoretical treatments to explain the event depth in terms of pore dimensions, the nature of the problem requires that assumptions be made, such as $D \ll L$ and $d \ll D$, to reach an analytical solution.[16] These assumptions can be reasonable for high aspect ratio pores, but are inapplicable to those with low aspect ratio. While our systems violate these assumptions as well, our experiments provide a bridge between the high and low aspect ratio regimes and have enabled us to use previous treatments to develop an empirical model consistent with our findings.

Recall that the pore's resistance dictates the magnitude of the ionic current in response to an applied voltage and this resistance is the sum of the pore's geometrical and access resistance as shown in eq 4. Recent work by Tsutsui *et al.* using microscale pore diameters in 50 and 400 nm-thick membranes suggests that the access resistance is largely unaffected during particle translocation.[25] To further investigate this hypothesis, we turned to the resistive pulse analysis of DeBlois and Wesley, who introduced a parameter α to compensate for external resistances, R_{ext}, which are resistances in the system not stemming from the pore.[17]

$$\alpha = \frac{R_{ext}}{R} \tag{7}$$

In the limit that the access resistance is completely unaffected by the particles, it can be treated independently of the pore's geometric resistance, essentially behaving as an external resistance. Making the appropriate substitutions, eq 7 becomes

$$\alpha = \frac{R_a}{R_p} = \frac{\pi D}{4L} \tag{8}$$

To complete our assessment, we include the coefficient β to address the distinct cases of whether the particle's

diameter is larger or smaller than the length of the pore. Briefly, this factor accounts for the distortion of the electric field lines inside the pore created by the presence of a particle. As such, it is a function of both the pore and particle geometries. For a more complete discussion of this effect, we refer the reader to the works of DeBlois and Bean and also Gregg and Steidley, from which we have gleaned the following values:[16,35]

$$\beta = \begin{cases} 1, d \geq L \\ \frac{3}{2}, d < L \end{cases} \quad (9)$$

It is unlikely that β is discontinuous in this fashion; however, determining precise values would require numerical simulations and we have found that the straightforward approximation of eq 9 is sufficient to describe our results.

On the basis of these considerations, we can express i_{mp} in terms of the geometries of the pores and particles as:

$$i_{mp} \approx \frac{\beta\chi}{1+\alpha} = \begin{cases} \frac{d^3}{\left(L+\frac{\pi D}{4}\right)D^2}, d < L \\ \frac{2d^3}{3\left(L+\frac{\pi D}{4}\right)D^2}, d = L \\ \frac{2Ld^2}{3\left(L+\frac{\pi D}{4}\right)D^2}, d > L \end{cases} \quad (10)$$

We again plot the mean event depths, but with the abscissa values being given by $\beta\chi/(1 + \alpha)$, shown as filled markers in Figure 3a–c. Figure 3d shows the σ_i plotted against $\beta\chi/(1 + \alpha)$; the linearity of this plot supports our earlier claim that the standard deviation is related to the particle size distribution. Shrinking the pore results in larger σ_i values and accounting for the invariance in access resistance results in one line fitting data from each membrane thickness. Returning to the most probable event depth *versus* $\beta\chi/(1 + \alpha)$, the analysis is identical to that presented for i_{mp} versus χ; however, we will subscript the linear fit parameters with α; that is, $i_{mp} = m_\alpha[\beta\chi/(1 + \alpha)] + b_\alpha$. By inspection, the b_α values are once again within experimental uncertainty of 0 except for L_{500} and, in each case, $b = b_\alpha$ (again, within experimental uncertainty). This further strengthens the hypothesis that this offset is a consequence of systematically underestimating χ for thick pores. With the values of m_α being consistent across the membrane thicknesses and very nearly unity, we believe we have captured the most relevant parameters in describing the ionic current through a pore device in response to translocating particles. We would like to point out that the formulation for $d < L$ agrees with that proposed by Sun and Crooks for micrometer-long carbon nanotube-based Coulter counters.[23]

While the results shown in Figure 3 clearly support the hypothesis of invariant access resistance during particle translocation proposed by Tsutsui *et al.* and suggest that this is a relevant concern in even longer pores, we caution the reader not to place too much emphasis on the length itself.[24] Rather, the inclusion of $(1 + \alpha)^{-1}$ demonstrates the pore's aspect ratio is the more relevant parameter. That the access resistance is largely unaffected by particle translocations also suggests that interactions near and inside the pore itself are responsible for determining even depth. As will be shown, these interactions are mediated by the electric field in the vicinity of the pore, which is also intimately related to a pore's aspect ratio.

Event Duration. As discussed previously, the resistive pulse detection scheme relies on the characterization of translocation events by their intensity and duration. While the event depth affords insight into a particle's size relative to the pore, studying the event duration can provide information on a particle's charge. Chemically distinct particles of the same size cannot be distinguished solely by event depth analysis; however, if these unique chemistries result in differences in surface charge, event duration can provide distinction where event depth cannot. Particles possessing higher charge will have stronger interactions with an applied electric field, meaning their translocation velocities will differ from particles of lower charge and will be measured as different event durations. These differences can be then used to determine the magnitude of the surface charge.[30] Furthermore, the distribution of translocation times can be used to reveal the nature of interactions between the analyte and the pore itself.[36]

Recently, Bacri *et al.* used this approach to identify three distinct types of events for silica nanoparticles of a single size translocating 180 nm diameter pores in 50 nm thick silicon nitride membranes: short, medium, and long events.[26] The first case is attributed to particle collisions with the pore; that is, a particle approaches the pore but does not completely translocate through it. Long events are interpreted as one particle entering the pore as another exits, meaning they are essentially observing two successive events with no resolvable temporal separation. Finally, the medium-duration events are indicative of traditional translocation. In our experiments, all three behaviors were observed but only "normal" translocation events (*i.e.*, single particles, medium-event duration) were included for analysis. For a detailed discussion of how events were categorized, we refer the reader to the Supporting Information. A fourth possibility for a particle having entered a pore is that it simply does not exit: that is, the particle becomes stuck inside the pore. Stuck particles could frequently be ejected by reversing the polarity of the applied electric potential; however, every translocation experiment does ultimately end with a particle irreversibly clogging the pore.

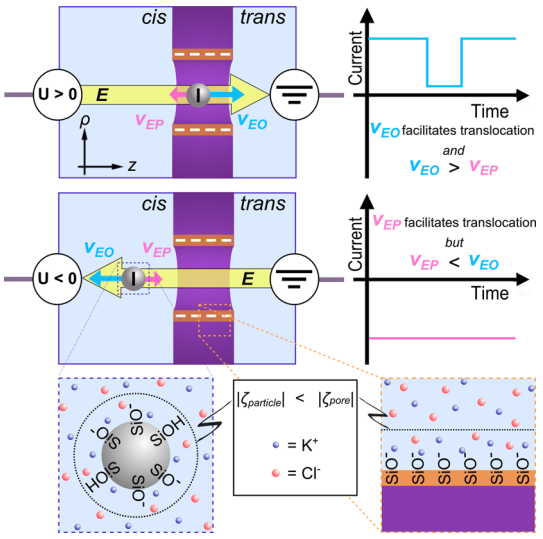

Scheme 2. Electrokinetic phenomena responsible for particle translocation. White circles represent the Ag/AgCl electrodes used to source a voltage across the membrane. When the applied voltage is positive, the electric field points from the *cis* to the *trans* side of the membrane. As the particle is negatively charged, its electrophoretic velocity, v_{EP}, frustrates translocation, but the electro-osmotic velocity resulting from the negative surface charge of the pore, v_{EO}, is sufficient to overcome v_{EP} and the particle moves through the pore. When the polarity reverses, so too does the direction of the electric field and v_{EO} suppresses translocation. The electric field always points in the direction of decreasing electric potential difference. The zeta potentials of both the particles and the pore determine which electrokinetic transport phenomenon will dominate. In both cases, the zeta potential will depend on surface charge as well as the pH and ionic strength of the solution. Because of an aggressive oxidizing pretreatment (see Methods), the pore's zeta potential is more negative than that of the particles and EO is responsible for particle transport.

This clogging problem is not unique to our pores and is indeed the subject of ongoing research.[37] Generally speaking, the approach adopted to combat this fouling in silicon nitride pores is to functionalize the surface through chemical modifications. We elected an easier, lower-cost alternative in this study, involving the enhancement of the negative surface charge of both the pore and particles by simply working at an elevated pH value of 10 to strengthen the electrostatic repulsion between the two. Silicon nitride's surface chemistry is quite similar to silicon oxide: for thin films, it has been shown that upward of 98% of the surface groups are silanes.[38] At pH 10, we expect the large majority of these groups to be deprotonated (as shown in the lower panels of Scheme 2). A somewhat surprising consequence of this elevated surface charge is the resulting electro-osmotic (EO) flow through the pore is sufficient to transport particles and virtually eliminate electrophoretic (EP) translocation, which is typically employed in pore sensing platforms. Scheme 2 is presented to help visualize the electrokinetics of our system: The EP component of a particle's motion is the response of the charged particle to the applied electric field which is created by the applied electric potential difference across the membrane, *U*. The field is a vector which points in the direction of decreasing potential. Because our particles are negatively charged, their EP motion will be antiparallel to the electric field. Electro-osmosis is the motion of the solvent coupled to the ionic motion. The pore's negative surface charge enhances the cation concentration inside the pore, thus when an electric field is applied, their motion generates fluid flow parallel to the applied field. For a more detailed discussion on the electrokinetics in nanopores, the reader is referred to the work of Schoch *et al.*[39]

Having a qualitative understanding of the interactions responsible for the particle's motion, we now turn to a more focused analysis of our data to explore what information can be gained to develop a more quantitative description. In the presence of a field, the resulting electrokinetic velocity components can be expressed in the following way:

$$\mathbf{v}_{EP} = \frac{\varepsilon}{\eta}\zeta_{particle}\mathbf{E} \quad (11)$$

$$\mathbf{v}_{EO} = \frac{\varepsilon}{\eta}\zeta_{pore}\mathbf{E} \quad (12)$$

Summing eqs 11 and 12 will give the resultant velocity vector:

$$\mathbf{v} = \mathbf{v}_{EP} + \mathbf{v}_{EO} = \frac{\varepsilon}{\eta}(\zeta_{particle} - \zeta_{pore})\mathbf{E} \quad (13)$$

where **v** is the velocity, ε is the product of the permittivity of free-space and the dielectric constant of water (the solvent), η is the viscosity of water, ζ represents the zeta potential of the pore or particle (note the subscripts in eqs 11−13), and **E** is the magnitude of the electric field (boldfaced variables represent vector quantities).[39] Briefly, the zeta potential is the electrostatic potential at the boundary between the immobile counterions surrounding a charged surface and the freely diffusing bulk phase (illustrated in the bottom panels of Scheme 2). Thus, it is intimately related to the surface charge and ionic strength of the electrolyte, but provides a more convenient quantity to work with as the zeta potential of the nanoparticles can be readily measured using electrophoretic light scattering (or ELS, see Methods section).

As suggested by Scheme 2, we will assume that the velocity is solely in the +*z*-direction (from the *cis* chamber to the *trans* side of the membrane). Zeta potentials were found to be $\zeta_{d50} = -26.0 \pm 3.0$ mV and $\zeta_{d100} = -33.9 \pm 3.0$ mV for the 50 and 100 nm particles, respectively. Combining an expression developed by Yusko *et al.* with the zeta potential found for silicon nitride at pH 10 in 400 mM KCl in the Firnkes's report, we can estimate the zeta potential of the pore in 100 mM KCl at pH 10, which was found to be $\zeta_{pore} = -44.0$ mV.[40,41] We rewrite eq 13 to emphasize EO

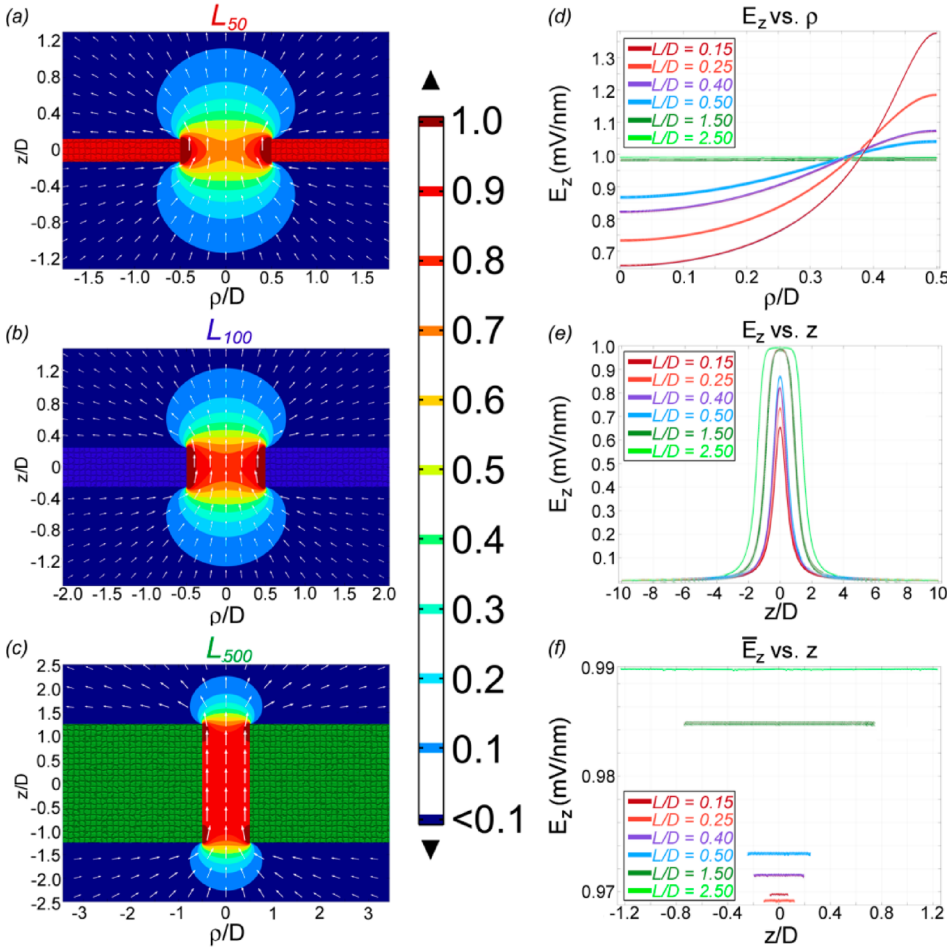

Figure 4. (a–c) Finite element analysis calculations for the *z*-component of the electric field, E_z, are shown as contours for the three membrane thicknesses. Membranes are textured and colored for easy identification. White arrows indicate the direction of the field. The voltage is $U = L + \pi D/4$ mV for facile comparison to eq 15. A field magnitude of 1 mV/nm represents regions where our approximation is most valid. (d) The variation of the electric field strength over the radial direction, ρ, scaled in terms of pore diameter along the $z = 0$ radial line and (e) in the *z*-direction at $\rho = 0$. Note that the origin is taken to be the center of the pore. Our approximation is most valid for higher aspect ratio pores; however, in panel f we see that the average value E_z over the circular cross sections of the pore is very nearly 1 mV/nm.

dominates EP and that we have reduced the problem to one dimension:

$$v_z = \frac{\varepsilon}{\eta}(|\zeta_{pore}| - |\zeta_{particle}|)E_z \qquad (14)$$

We are now left only to determine expressions for the particle velocity and the electric field in the *z*-direction, v_z and E_z, respectively.

Despite the heightened nanopore surface charge, we do not believe the resulting static electric field strongly influences the translocation times. Rather, its primary role is to frustrate silica particles from clogging the pore should they approach its surface. Counterions present in the electrolyte screen this surface charge over the Debye length, which is on the order of 1 nm in 100 mM KCl (the electrolyte used in our experiments). Therefore, the only electric field we have considered, in terms of eq 14, is a consequence of the applied voltage. Since the driving force in and around the pore will be closely related to the voltage drop across the pore's length, or U_p, U_p/L seems a reasonable approximation for E_z:

$$E_z = \frac{U_p}{L} = \frac{U\left(\frac{R_p}{R}\right)}{L} = \frac{U}{L + \frac{\pi D}{4}} \qquad (15)$$

Using finite element simulations, we were able to verify that this is in fact a reasonable estimate; however, it is important to mention that this approximation neglects significant edge effects and radial variations of the field within the pore as shown in Figure 4. By using $U = L + \pi D/4$ in the simulations, we are able to easily compare their results to our approximation. Substituting $L + \pi D/4$ in eq 15 returns 1, meaning the approximation is most valid for cases where the field strength is nearly 1 mV/nm in the simulation results. In panels a–c of Figure 4, the magnitude of E_z is shown as contours in and around the pore. Note that the electric field strength drops to less than 10% of its maximum

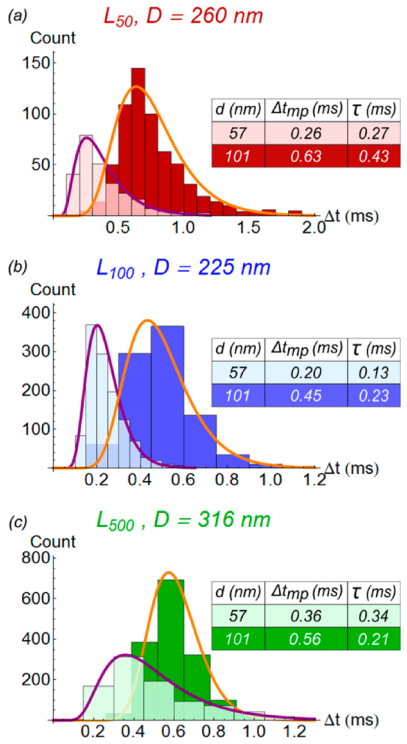

Figure 5. Translocation time distributions are shown for (a) L_{50}, (b) L_{100}, and (c) L_{500} pores. For panels a and b, $E_z \approx$ 0.3 mV/nm while the results of panel c were obtained at $E_z \approx$ 0.2 mV/nm. Inverse Gaussian fits are shown in purple for the d_{50} particles (lighter bars) and log-normal curves are orange for the d_{100} particles (darker bars). However, each particle size is fit with both PDFs, and the resulting Δt_{mp} and τ values are averaged.

value at a distance of ~1 pore diameter away from the pore entrance/exit. Inside the pore near $\rho = 0$, a fairly uniform region of E_z does exist with a magnitude within roughly 30% of eq 15, but significant radial and axial variations do exist, as shown explicitly in panels d and e, respectively. These variations are most pronounced in the lowest aspect ratio pores. However, if the value of E_z is averaged over cross sections along the pore axis, we see that the value is very nearly 1 in all examined pore geometries. Put another way, panels d and e can be seen to show the limitations of the approximation, especially in low aspect ratio pores, while panel f confirms that it is a physically meaningful quantity.

Turning to the particle velocity, we present Figure 5 as an example of the duration distributions for translocation times, or Δt, for the three pore thicknesses at $U = +150$ mV. The distribution of Δt values corresponds to a distribution of particle velocities, but it is immediately evident from the shape of the plots that there is a most probable translocation time, Δt_{mp}, and, hence, a most probable velocity, v_{mp}. Note that for durations greater than the most probable translocation time ($\Delta t > \Delta t_{mp}$), the distribution decays in an exponential fashion. For this reason, we have defined τ as a time-constant-like parameter such that the probability of an event having $\Delta t = \Delta t_{mp} + \tau$ is equal to the probability at Δt_{mp} divided by the base of the natural logarithm, e. While Δt_{mp} is the more relevant parameter in terms of analyzing the particles, τ is useful for identifying experiments dominated by the long-type events mentioned previously. A more detailed discussion of how this is accomplished can be found in the Supporting Information.

The following analysis is nearly identical to that used in the previous section: we are once more interested in the PDF that best describes our distributions such that we can determine the parameters Δt_{mp} and τ. As the distribution clearly involves an exponential decay, we restrict our search to functions from the exponential family. We chose to focus on two for this study: the log-normal distribution (LN) and the inverse Gaussian distribution (IG):

$$P_{LN}(\Delta t) = \frac{C_1}{s_1 \Delta t \sqrt{2\pi}} e^{-(\ln \Delta t - a_1)^2/(2s_1^2)} \quad (16)$$

$$P_{IG}(\Delta t) = C_2 \sqrt{\frac{s_2}{2\pi \Delta t^3}} e^{-s_2(\Delta t - a_2)^2/(2a_2^2 \Delta t)} \quad (17)$$

where the C values are constants related to the total number of counts for a given experiment, the a values are related to the mean of the distribution, and the s parameters are tied to the shape of their respective PDFs. Once these parameters are identified, the derivative of the PDFs can be taken to identify the point at which they reach their maxima, Δt_{mp}, and the point at which they decay to 1/e of their maxima, $\Delta t_{mp} + \tau$. Similar to the σ_i value of the event depth histograms, τ gives an idea of the width of the duration distribution. However, an important difference between σ_i and τ is that the Δt distribution is always skewed toward higher values; that is, the shape of the distribution does not reflect that of the particle sizes as seen with the event depth histograms.

Before finalizing the velocity analysis, let us briefly comment on the PDFs themselves. When the logarithm of the variable of interest, in this case, the translocation time, is distributed according to a Gaussian or normal distribution, the variable itself is lognormally distributed. Event durations for carbon nanotubes and nucleosomal substructures moving through nanopores have been shown to be described well by LN distributions.[42,43] For the former, it was suggested that this distribution was also related to the length distribution of the nanotubes. By inspection (refer to Figure 2d), a similar argument could be made for the d_{50} particles used in our experiments, but clearly breaks down when applied to the d_{100} particles. The IG distribution is known to describe the motion of particles under the influence of a force introducing a drift component in the same direction as the net diffusive motion (distributions were identified independently by Schrödinger and Smoluchowski in 1915, although

these were not formalized until decades later).[44] Both PDFs were found to characterize the shape of our distributions well and since neither one "outperformed" the other in terms of statistical significance tests (see Methods section), the Δt_{mp} and τ resulting from the LN and IG fits were averaged.

The most probable translocation time allows us to define the most probable translocation velocity:

$$v_z = v_{mp} = \Delta z/\Delta t_{mp} \quad (18)$$

where Δz is the distance the particle travels during the event. Simulations performed by Prabhu *et al.* have found that the ionic current begins to fall from its baseline value, or that the translocation event starts, when the particle is approximately one pore diameter away from the pore mouth.[27] By symmetry, then, the event concludes once the particle is one pore diameter away from the pore exit. Thus, $\Delta z = 2D + L + d$, and substituting into eq 18 gives:

$$v_{mp} = (2D + L + d)/\Delta t_{mp} \quad (19)$$

Interestingly, from our simulations, we note that the magnitude of the *z*-component of the electric field drops to 10% of its maximum value within roughly one pore diameter away from the pore mouth. Supporting what we saw in the event depth analysis, this implies that it is only interactions that take place within the neighborhood of the pore (defined by D) that are significant in resistive pulse sensing, which is another way of stating the access resistance is not significantly affected by the particles.

While we expected a monotonic increase of v_{mp} with E_z, that is not the case as shown in Figure 6 where v_{mp} is averaged over 0.1 mV/nm intervals in E_z for each membrane thickness. The particles also appear to translocate at higher velocities through 500 nm pores at lower E_z values compared to the shorter pores; we believe this to be a consequence of the shortcomings of eq 15 discussed earlier. However, that is not to say nothing valuable came of this analysis. Clearly, 50 nm particles translocate significantly faster than 100 nm particles, demonstrating that electro-osmotic transport can be utilized as an effective means of slowing the translocation of highly charged particles. Furthermore, the large number of experiments performed allows for the determination of average ζ values; for a pore-based device, however, one would want to achieve reliable results with minimal runs.

Nonetheless, using eq 14 to calculate ζ_{pore} treating the $\zeta_{particle}$ values as known quantities, we find an average value of $\zeta_{pore} = -41.6 \pm 8.1$ mV. While this is in excellent agreement with the estimation of ζ_{pore} presented earlier in this section (*i.e.*, $\zeta_{pore} = -44.0$ mV), the uncertainty is quite large, which is reflective of the wide range of velocities measured at similar E_z values, which can be seen in the error bars of the charts presented in Figure 6. If we assume ζ_{pore} is fixed at -44.0 mV

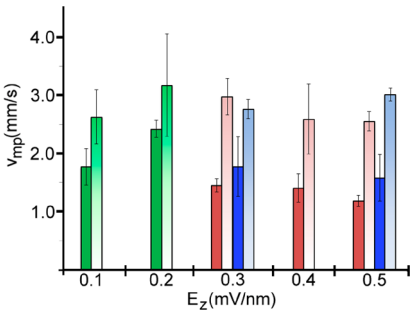

Figure 6. Velocities are averaged over E_z bin sizes of 0.1 mV/nm and shown for d_{50} (lighter bars) and d_{100} experiments (darker bars). Despite the large uncertainty, we can still determine that d_{100} particles translocate significantly slower than the d_{50} particles and calculate $\zeta_{particle}$ values that agree with ELS measurements. Interestingly, there is no discernible trend in particle velocity with either E_z or membrane thickness.

to calculate $\zeta_{particle}$, we find values consistent with independent measurements: $\zeta_{d50} = -31.2 \pm 6.8$ mV and $\zeta_{d100} = -33.9 \pm 8.4$ mV, compared to $\zeta_{d50} = -26.0 \pm 3.0$ mV and $\zeta_{d100} = -33.9 \pm 3.0$ mV from ELS.

Capture Rates. The rate at which events occur, or the capture rate, is also a critical consideration. This will determine how long an experiment must be run in order to record enough events to obtain meaningful statistics (typically several hundred). To determine the capture rates in each of our experiments, the time between successive events, *T*, is tracked and the resulting distribution is plotted as shown below in Figure 7. When the particles do not interact with one another, these distributions can be fit with an exponential decay of the form:

$$P(T) = Ce^{-fT} \quad (20)$$

where *f* is the capture rate and *C* is a constant such that $\int_0^{T_{max}} P(T)\,dT = n$, the total number of events in a given experiment. The three rates expressed in Figure 7 are fairly representative of all experiments; that is, event frequencies were on the order of 1−10 Hz. Taking the bead concentration into consideration (10^9 to 5×10^{10} particles/mL), this is nearly identical to capture rates reported for electrophoretic nanoparticle translocation. As particle concentration increases, so does the event frequency. Bacri *et al.* measured rates that were 10−100 times higher than ours with silica particles in thin silicon nitride pores with ~100 times higher bead concentration.[26] Similarly, observing polystyrene beads translocations in a CNT-based apparatus, Sun and Crooks were able to capture up to 20 polystyrene particles/s using a concentration of 5×10^{11} particles/mL.[29]

In addition to the concentration, the rate at which particles are delivered to the pore, which is controlled by their electric field driven motion, will also influence event frequency. We again encounter the important distinction of scale in our system. In the event depth

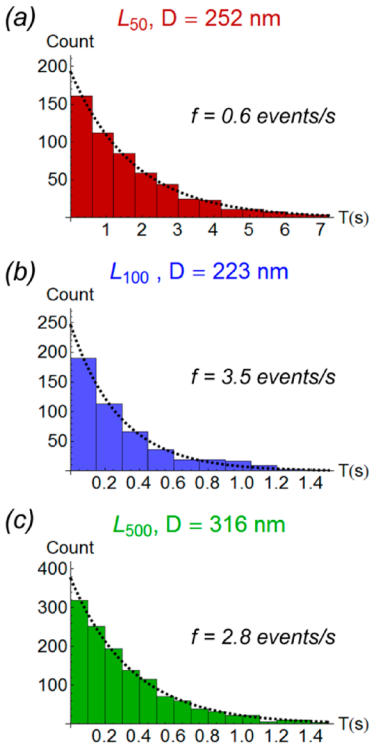

Figure 7. Distributions for the time between successive events, *T*, are plotted for the three membrane thicknesses. Each experiment shown was performed at $\xi \approx 0.15$ Hz/mV using d_{100} particles; *f* is determined by fitting histograms with an exponential decay $\sim e^{-fT}$.

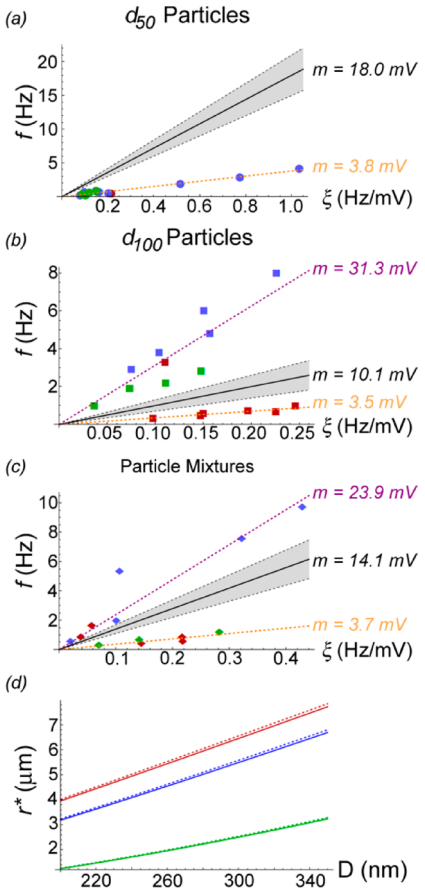

Figure 8. (a–c) Capture rate, *f*, is plotted for d_{50} and d_{100} particles, along with mixture of the two. Black lines represent $|\zeta_{pore}| - |\zeta_{particle}|$ according to $\zeta_{pore} = -44$ mV and $\zeta_{particle}$ determined from ELS data. For the mixture, event frequency scales as $(C_{d50}/C_{tot})f_{50} + (C_{d100}/C_{tot})f_{100}$, where *C*s represent the concentration of the particles in the mixture. As $C_{d50} = C_{d100} = C_{tot}/2$, the slope of the theoretical line is given by $(2|\zeta_{pore}| - |\zeta_{d50}| - |\zeta_{d100}|)/2$. Slope values are shown for the best fit line. There are clearly high and low capture rate regimes for 100 nm particles and the mixtures, with all of the L_{100} experiments belonging to the high frequency regime. Beyond that, it is unclear if there are any signs of capture rate dependence on pore length. The capture radius, *r, is plotted as a function of pore diameter for different particle size and membrane thickness combinations inpanel d. Dashed lines are for d_{50} particles and solid lines are for d_{100} beads. The lines for the different sized particles nearly overlap as $\delta_{d50}/\delta_{d100} \approx (|\zeta_{pore}| - |\zeta_{d100}|)/(|\zeta_{pore}| - |\zeta_{d50}|)$. Because *f* scales linearly with *r**, this plot suggests that thinner pores have higher capture rates, but we do not see this in our experiments.**

and event duration sections, we found that only interactions in the immediate vicinity of the pore (*i.e.*, within one pore diameter) played an important role; however, the rate at which particles enter this region will be controlled by the field outside of it. Wanunu *et al.* and Wong and Muthukumar developed analytical expressions for this rate in the cases of pure electrophoresis and electro-osmosis, respectively, which we can combine to develop a more complete treatment for the electrokinetics outside the pore, and ultimately the capture rate.[45,46] Central to both studies is the concept of a capture radius. A particle is said to have entered the capture radius of the pore once its random diffusive velocity is overcome by directed, field-driven motion. Letting *r* represent the radial distance from the center of the pore, we choose to write velocities for $r > D$ as υ rather than v to avoid confusion. We also assume solvent and current flow is in the radial direction alone.

The electroosmotic component of this motion, $\upsilon_{EO}(r)$, is a result of the continuity of fluid flow: the fluid flux into the pore must be equal to the flux out of the pore.

$$\upsilon_{EO}(r) = \frac{A_{pore} v_{EO}}{2\pi r^2} = \frac{\varepsilon|\zeta_{pore}|UD^2}{8\eta\left(L + \frac{\pi D}{4}\right)r^2} \qquad (21)$$

where A_{pore} is the cross-sectional area of the pore. Just as before, the electrophoretic component, $\upsilon_{EP}(r)$, is simply the motion resulting from the field acting on the charge of the particle; however, we must remain aware that this is the field outside of the pore, which we will call E_{cis}.

$$E_{cis}(r) = -\frac{\partial U_{cis}}{\partial r} = I\frac{\partial R_{cis}}{\partial r} = \frac{\pi\kappa UD^2}{4L + \pi D}\left(\frac{\partial R_{cis}}{\partial r}\right)$$

$$= \frac{\pi\kappa UD^2}{4L + \pi D}\left(\frac{\partial r}{2\pi\kappa r^2 \partial r}\right) = \frac{UD^2}{2(4L + \pi D)r^2} \qquad (22)$$

The above utilizes the resistance of a vanishingly thin hemispherical shell, $\partial R = \partial r/(2\pi\kappa r^2)$, and the fact that the direction of current flow is opposite of ∂r, accounting for

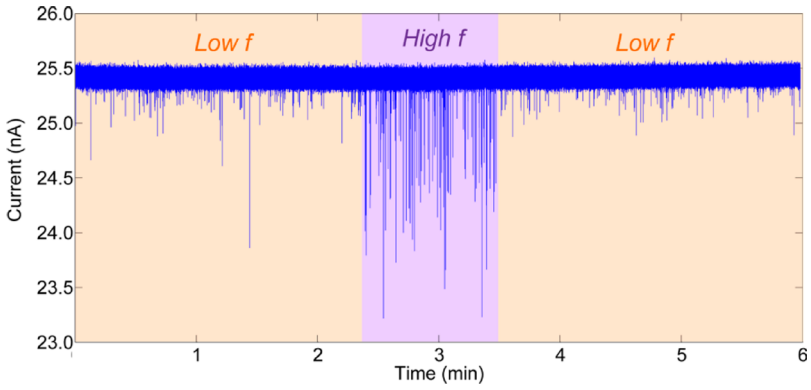

Figure 9. A mixture of 2 × 10^{10} d_{50} and d_{100} particles/mL (10^{10}/mL each) in a D = 215 nm, L_{100} pore at 150 mV. Within one 6 min experiment, both low and high capture rates are demonstrated. In the low frequency portions, the events are primarily due to d_{50} particles, whereas many more d_{100} (deeper) events are seen in the high frequency section. While this indicates that f is intimately tied to the particle being detected, it is unclear exactly how particle parameters contribute to event frequency at this point.

the disappearance of the negative sign with the introduction of I.

$$v_{EP}(r) = -|\zeta_{particle}|E_{cis}(r) = -\frac{\varepsilon|\zeta_{particle}|UD^2}{2\eta(4L+\pi D)r^2} \quad (23)$$

Rounding out the pertinent velocities is the diffusive velocity of particle on the length scale r, which is given by

$$v_{dif}(r) = \frac{\delta}{r} \quad (24)$$

where δ is the particle's diffusion coefficient. At the capture radius, r^*,

$$v_{EO}(r^*) + v_{EP}(r^*) = \frac{\delta}{r^*} \quad (25)$$

Substituting and solving for r^* gives

$$r^* = \frac{\varepsilon UD^2}{2\eta\delta(4L+\pi D)}(|\zeta_{pore}| - |\zeta_{particle}|) \quad (26)$$

For a perfectly absorbing hemisphere of radius r^*, the capture rate is

$$f = 2\pi N_c \delta r^* = \frac{\pi N_c \varepsilon UD^2}{\eta(4L+\pi D)}(|\zeta_{pore}| - |\zeta_{particle}|) \quad (27)$$

with N_c being the number of particles per cubic meter. To simplify notation, we let $\xi = (\pi N_c \varepsilon UD^2)/(\eta(4L + \pi D))$. While this simplification could be achieved by expressing the right-most side of the equation in terms of E_z or even v_{mp} from the previous section, we intentionally present it in this manner to again stress that it is a result of considering interactions that take place outside the pore vicinity. Indeed, as we show in Figure 8d, the capture radius can be more than an order of magnitude larger than the pore diameter. On the basis of eq 27, it once again appears that the quantity of interest will depend on the difference between the zeta potential of the pore and that of the particles. In Figure 8, we show the measured capture rates *versus* ξ, along with theoretical capture rates using the $\zeta_{particles}$ measured by ELS and ζ_{pore} calculated from the data of Firnkes *et al.* for (a) d_{50} particles, (b) d_{100} particles and (c) mixtures of the two.[40,41] Event depth and duration data from bead mixture experiments can be found in Supporting Information. The capture radii in Figure 8d have also been calculated using the same zeta potentials. That r^* is virtually identical for d_{50} and d_{100} particles might be surprising at first glance, but it is expected as $\delta_{50} = 2\delta_{100}$ and $(|\zeta_{pore}| - |\zeta_{d50}|) \approx 2(|\zeta_{pore}| - |\zeta_{d100}|)$.

Returning to panels a–c of Figure 8: with $f = (|\zeta_{pore}| - |\zeta_{particle}|)\xi$, the slope is expected to be the difference between $|\zeta_{pore}|$ and $|\zeta_{particle}|$ or 18.0 mV for d_{50} particles and 10.1 mV for d_{100} particles. In the case of the mixtures, the total frequency is equal to the sum of the individual frequencies. For the experiments shown in Figure 8c, equal concentrations of d_{50} and d_{100} particles were used. Thus, the expected slope in this case is given by $^1/_2(2|\zeta_{pore}| - |\zeta_{d50}| - |\zeta_{d100}|) = 14.1$ mV. In each case, there is substantial disagreement between these theoretical values and slope of the line(s) used to fit the experimental data. The disagreement with theory is not altogether unexpected considering the theoretical capture rates are approximations developed for pores of similar lengths to ours, but 1 to 2 orders of magnitude smaller in diameter. Strikingly, this disagreement goes both ways. There appear to be two distinct capture rates when 100 nm particles are present in the solution: one which is roughly $^1/_3$ of the expected value and the other 2–3 times the theory.

Unfortunately, in the context of these experiments we are unable to definitively comment on whether this is a consequence of a poor approximation, poorly defined zeta potentials, or if something more interesting is happening in our system. Shown in Figure 9 is a trace in which both low and high capture rates are seen in the same experiment, which would suggest that one of the latter two explanations is more likely than the first. That the 100 nm particles seem to be capable of higher translocation rates than the more modestly charged 50 nm particles and that the larger particles do not fall on the lower capture rate curve for L_{100}

membranes are also intriguing, but again, at present these remain curiosities. Tuning the nanopore surface potential *via* an embedded gate electrode, which has been discussed in recent studies, would provide an excellent route to investigate this further.[47,48]

CONCLUSIONS

We have presented resistive pulse analysis over a range of nanopore diameters and lengths providing more evidence that a pore's access resistance remains unaffected by translocating particles in agreement with the findings of Tsutsui *et al*. in ultralow aspect ratio pores.[26] By investigating the contribution of access resistance over this range of pore aspect ratios and building on the analysis for high aspect ratio pores, we are able to formulate an approximation for the response of the ionic current to a translocating particle which mathematically accounts for this in terms of the pore geometry relative to the particle size.

To further probe the influence of pore geometry, we studied event durations and particle capture rate as both depend heavily on the electric field that results from the applied voltage and pore aspect ratio. We were able to develop relevant approximations for this field through an understanding of the electrokinetic transport phenomenon responsible for particle translocation, namely electro-osmosis and electrophoresis. In so doing, we demonstrated that event durations can be used as a measure of particle or pore zeta potential when electro-osmotic transport dominates and that electro-osmosis provides an effective means of driving particles through a pore and slowing the translocation velocity of heavily charged particles.

In terms of event magnitudes and durations, we have shown that the most important interactions appear to take place not just within the pore, but within a region that extends to one pore diameter on either side of the pore regardless of aspect ratio. Our capture rate analysis reveals more work is needed to identify the nature of interactions outside this region to optimize the particle capture rate, which was found to be both lower and higher than anticipated and may be related to the pore aspect ratio. These findings provide valuable considerations when designing a pore sensor for a target analyte of a particular size or charge, but also illustrate how pores can be used singly or potentially networked in series or parallel to address unknown particles.

METHODS

Aqueous electrolyte solutions were composed of 100 mM potassium chloride (Fluka) with 10 mM TRIZMA base (Sigma), buffered to pH 10 with KOH (Mallinckrodt), and were prepared using double-distilled water filtered through cellulose nitrate filter membranes (Nalgene, 200 nm pore size). Unless otherwise noted, all chemicals were used as received. After the addition of salts and buffering, electrolyte solutions were filtered twice more using polycarbonate filter membranes (Steriltech Corporation, 100 nm pore size). Solutions containing 50 and 100 nm silica nanoparticle (Polysciences, Inc.; size verified by SEM) were prepared by the serial dilution of the stock suspension ($\sim 10^{14}$ particles/mL for 50 nm particles and $\sim 10^{13}$ particles/mL for 100 nm particles) into the filtered electrolyte until the desired bead concentration was reached (10^9 to 5×10^{10} particles/mL for this report). To prevent aggregation of the silica beads, suspensions were sonicated for 2 min following the addition of the beads, then gently agitated overnight using a rotary mixer and finally sonicated again for 1 min immediately before use. Nanoparticle samples used for zeta potential measurements were prepared in the same manner. A Malvern Zetasizer Nano ZS90 was used to determine zeta potentials using electrophoretic light scattering (ELS). A nanoparticle suspension is loaded into a clear U-shaped, cell with electrodes at either end. A voltage is applied to drive particles through a laser passing through the cell into a photodetector. Fluctuations in the intensity of the laser light that reaches the detector can be used to determine the electrophoretic mobility of the particles and is used to calculate their zeta potential.

Silicon nitride samples were furnished by Silson Ltd. (Northampton, UK) in the form of 5 mm $\times$ 5 mm chips with three different membrane thicknesses: 50, 100, and 500 nm. Silicon nitride layers are grown *via* low pressure chemical vapor deposition (LPCVD) on both sides of a silicon support wafer. Using standard photolithographic techniques followed by plasma etching, a small portion of one of the silicon nitride layers is removed. The exposed silicon is then etched with KOH, leaving a free-standing silicon nitride membrane. In this study, the membrane section accounted for an area of roughly 100 μm $\times$ 100 μm on the chip.

Nanopores were milled in the free-standing membranes using a focused ion beam (FIB). Prior to milling, the membranes were sputter coated with a thin ($\sim$10 nm) layer of gold to prevent accumulation of charge during ion milling and electron imaging. Two different instruments were employed for this study: an FEI Nova Dual Beam System (Lawrence Livermore National Lab) and a Zeiss 1540xB Cross Beam System (Lawrence Berkeley National Lab). The systems consist of two beams: an ion beam for milling (gallium ions are accelerated to 30 keV to ablate a target with nanoscale precision) and an electron beam for imaging; thus, a pore could be drilled and imaged/measured immediately afterward. The choice of instrument used was determined solely by availability. Through the preparation of several pores, milling parameters (ion beam current, spot size, mill depth, and exposure time) were established to fabricate pores with diameters between 50 and 600 nm to within $\pm$10% for both instruments; however, for this report, we focused on diameters in the range of roughly 200$-$300 nm.

Gold was removed from the chips using Gold Etch Type TFA (Transene Company, Inc.), each was cleaned twice in a room temperature solution of freshly prepared piranha solution consisting of 3:1 v:v 98% sulfuric acid (Fisher):30% hydrogen peroxide (BHD) for at least 4 h per cleaning and rinsed thoroughly after each cleaning with warm DI water. Please note that extreme care should be taken when working with piranha solution as it reacts explosively on contact with most organics. Chips were dried under nitrogen before being loaded into a custom polydimethylsiloxane (PDMS; Dow-Corning Sylgard 184) conductivity cell, which consisted of two compartments each containing a microfluidic channel.

When assembled, the pore represents the only connecting path between the two compartments/channels; that is, any fluid or ion flow between the chambers is through the nanopore. The entire PMDS/silicon nitride assembly was exposed to an air plasma at low power (Harrick PDC-001 at 7 W) for 30 s to facilitate wetting of the cell and pore before filling with 100 mM KCl, 10 mM TRIS (pH 10.0). Using a HEKA EPC-10 patch clamp

amplifier and Ag/AgCl pellet electrodes (A-M Systems) placed on both sides of the membrane, a voltage was sourced across the membrane while simultaneously measurement was made of the ionic current through the pore. Currents were recorded for voltages between −100 mV and 100 mV in 10 mV increments in both increasing and decreasing directions to ensure there was no hysteresis. All measurements were performed inside a dark Faraday cage (Warner Instruments) on a vibration isolation table (Kinetic Systems, Inc.) to minimize electromagnetic and mechanical interference. As expected, all pores measured in this study displayed linear $I-V$ curves. Using eq 4, we could calculate a pore diameter based on its measured resistance and compare this value to the diameter determined using SEM measurements.

Upon successful verification of the pore diameter, the electrolyte in one chamber was replaced with a suspension of silica nanoparticles prepared as described above. The patch clamp amplifier was used to provide a constant voltage across the membrane while continuously monitoring the current in time. Using on-board electronics, the analogue signal was filtered with a 10 kHz low-pass Bessel filter and digitized at 100 kHz. Bead translocation events were detected using software written in MATLAB (*The Mathworks,* R2010a; detection software by K. Healy). Briefly, the software scans the current traces, calculating mean values and standard deviations of the ionic current, and identifies an event when the current level falls below a user-defined number of standard deviations below the mean current. For detection purposes, this value was set between 4 and 5 (depending on the bead size, membrane thickness, pore diameter, *etc.*), but only those events that reached depths greater than 6 times the root-mean-square noise of an event-free interval (typical intervals were on the order of seconds, *i.e.*, $\gg$ event durations) were included for analysis. This factor was chosen to ensure that the most intense fluctuations in the current *not* due to a bead passage would be disregarded. Additionally, only events lasting longer than twice the rise time of the low-pass filter were included for analysis because shorter duration events may be distorted by the filter. The rise time is roughly $^1/_3$ of the inverse of the filter's cutoff frequency, 10 kHz in this case, so all events less than ~70 μs were disregarded.

All histogram construction and curve fitting was performed with *Mathematica (Wolfram,* v8). For event durations, *Mathematica* was also used to determine the goodness of fit for log-normal and inverse Gaussian distributions using the Cramér-von Mises and Anderson-Darling tests. Referring to eqs 16 and 17, a and s parameters are calculated from considering all event duration data from an experiment and then substituting these values into appropriate equations. The resulting probability distribution is then compared to each individual data point and results are tabulated to evaluate the likelihood of the distribution describing the experiment. When a test returns a statistical significance, that is, the probability that the data matches the PDF purely by chance, of less than 5% for a given PDF, the hypothesis that the data is distributed according to that PDF is not rejected. Out of 122 tests—61 for both the Cramér-von Mises and Anderson-Darling tests—78 were not rejected for inverse Gaussian distributions (63.9%), while 79 were not rejected when compared to log-normal distributions (64.8%). Electric field distributions were calculated by numerically solving Poisson's equation for an insulating membrane using COMSOL v4.2.

Conflict of Interest: The authors declare no competing financial interest.

Acknowledgment. This work was performed under the auspices of the U.S. Department of Energy by Lawrence Livermore National Laboratory under Contract DE-AC52-07NA27344. This research was supported by the University of California Laboratory Fees Research Grant. This research was supported by the University of California Laboratory Fees Research Grant and the NSF (CHE 0747237). Portions of this work (pore fabrication) were performed as a User project at the Molecular Foundry, Lawrence Berkeley National Laboratory, which is supported by the Office of Science, Office of Basic Energy Sciences, of the U.S. Department of Energy under Contract No. DE-AC02-05CH11231. M. Davenport wishes to acknowledge the financial support of the Lawrence Scholars Program and the Achievement Rewards for College Scientists Foundation. K. Healy acknowledges the financial support of the European Union FP7Marie Curie Program (PIOF-GA-2008-220492). We acknowledge valuable discussions with Martin Langecker.

Supporting Information Available: A detailed discussion of the distinction between normal and anomalous translocation events along with results from experiments using pores to study suspensions containing both 50 and 100 nm silica particles. This material is available free of charge *via* the Internet at http://pubs.acs.org.

REFERENCES AND NOTES

1. Bayley, H.; Martin, C. R. Resistive-Pulse Sensing—From Microbes to Molecules. *Chem. Rev.* **2000**, *100*, 2575–2594.
2. Venkatesan, B. M.; Bashir, R. Nanopore Sensors for Nucleic Acid Analysis. *Nat. Nanotechnol.* **2011**, *6*, 615–624.
3. Kasianowicz, J. J.; Brandin, E.; Branton, D.; Deamer, D. W. Characterization of Individual Polynucleotide Molecules Using a Membrane Channel. *Proc. Natl. Acad. Sci. U.S.A.* **1996**, *93*, 13770–13773.
4. Manrao, E. A.; Derrington, I. M.; Laszlo, A. H.; Langford, K. W.; Hopper, M. K.; Gillgren, N.; Pavlenok, M.; Niederweis, M.; Gundlach, J. H. Reading DNA at Single-Nucleotide Resolution with a Mutant MspA Nanopore and Phi29 DNA Polymerase. *Nat. Biotechnol.* **2012**, *30*, 349–353.
5. Cherf, G. M.; Lieberman, K. R.; Rashid, H.; Lam, C. E.; Karplus, K.; Akeson, M. Automated Forward and Reverse Ratcheting of DNA in a Nanopore at 5-Å Precision. *Nat. Biotechnol.* **2012**, *30*, 344–348.
6. Dekker, C. Solid-State Nanopores. *Nat. Nanotechnol.* **2007**, *2*, 209–215.
7. Healy, K. Nanopore-Based Single-Molecule DNA Analysis: A Review. *Nanomedicine* **2007**, *2*, 459–481.
8. Healy, K.; Schiedt, B.; Morrison, A. P. Solid State Nanopore Technologies for Nanopore-Based DNA Analysis. *Nanomedicine* **2007**, *2*, 875–897.
9. Branton, D.; Deamer, D. W.; Marziali, A.; Bayley, H.; Benner, S. A.; Butler, T.; Di Ventra, M.; Garaj, S.; Hibbs, A.; Huang, X.; *et al*. The Potential and Challenges of Nanopore Sequencing. *Nat. Biotechnol.* **2008**, *26*, 1146–1153.
10. Wanunu, M. Nanopores: A Journey Towards DNA Sequencing. *Phys. Life Rev.* **2012**, *9*, 125–158.
11. Coulter, W. H.; Means for Counting Particles Suspended in a Fluid. US Patent No. *2656508*, **1953.**
12. Han, A.; Schürmann, G.; Mondin, G.; Bitterli, R. A.; Hegelbach, N. G.; de Rooij, N. F.; Staufer, U. Sensing Protein Molecules Using Nanofabricated Pores. *Appl. Phys. Lett.* **2006**, *88*, 093901–093903.
13. Skinner, G. M.; van den Hout, M.; Broekmans, O.; Dekker, C.; Dekker, N. H. Distinguishing Single- and Double-Stranded Nucleic Acid Molecules Using Solid-State Nanopores. *Nano Lett.* **2009**, *9*, 2953–2960.
14. DeBlois, R. W.; Bean, C. P.; Wesley, R. K. A. Electrokinetic Measurements with Submicron Particles and Pores by the Resistive Pulse Technique. *J. Colloid Interface Sci.* **1977**, *61*, 323–335.
15. Pevarnik, M.; Healy, K.; Toimil-Molares, Morrison, A.; Létant, S. E.; Siwy, Z. S. Polystyrene Particles Reveal Pore Substructure as They Translocate, *ACS Nano*, **2012**, published online July 15, 2012, doi: 10.1021/nn302413u.
16. DeBlois, R. W.; Bean, C. P. Counting and Sizing of Submicron Particles by the Resistive Pulse Technique. *Rev. Sci. Instrum.* **1970**, *41*, 909–916.
17. DeBlois, R. W.; Wesley, R. K. A. Sizes and Concentrations of Several Type C Oncornaviruses and Bacteriophage T2 by the Resistive-Pulse Technique. *J. Virol.* **1977**, *23*, 227–233.
18. Uram, J. D.; Ke, K.; Hunt, A. J.; Mayer, M. Submicrometer Pore-Based Characterization and Quantification of Antibody-Virus Interactions. *Small* **2006**, *2*, 967–972.
19. Lan, W.-J.; Holden, A. D.; Zhang, B.; White, H. S. Nanoparticle Transport in Conical-Shaped Nanopores. *Anal. Chem.* **2011**, *83*, 3840–3847.

20. Lan, W.-J.; Holden, D. A.; Liu, J.; White, H. S. Pressure-Driven Nanoparticle Transport across Glass. *J. Phys. Chem. C* **2011**, *115*, 18445–18452.
21. Lan, W.-J.; White, H. S. Diffusional Motion of a Particle Translocating through a Nanopore. *ACS Nano* **2012**, *6*, 1757–1765.
22. Zhou, K.; Li, L.; Tan, Z.; Zlotnick, A.; Jacobson, S. C. Characterization of Hepatitis B Virus Capsids by Resistive-Pulse Sensing. *J. Am. Chem. Soc.* **2011**, *133*, 1618–1621.
23. Sun, L.; Crooks, R. M. Fabrication and Characterization of Single Pores for Modeling Mass Transport across Porous Membranes. *Langmuir* **1999**, *15*, 738–741.
24. Kozak, D.; Anderson, W.; Vogel, R.; Chen, S.; Antaw, F.; Trau, M. Simultaneous Size and ζ-Potential Measurements of Individual Nanoparticles in Dispersion Using Size-Tunable Pore Sensors, *ACS Nano*, **2012**, published online July 25, 2012, doi: 10.1021/nn3020322
25. Tsutsui, M.; Hongo, S.; Hem, Y.; Taniguchi, M.; Gemma, N.; Kawai, T. Single-Nanoparticle Detection Using a Low-Aspect-Ratio Pore. *ACS Nano* **2012**, *6*, 3499–3505.
26. Bacri, L.; Oukhaled, A. G.; Schiedt, B.; Patriarche, G.; Bourhis, E.; Gierak, J.; Pelta, J.; Auray, L. Dynamics of Colloids in Single Solid-State Nanopores. *J. Phys. Chem. B* **2011**, *115*, 2890–2898.
27. Prabhu, A. S.; Jubery, T. Z. N.; Freedman, K. J.; Mulero, R.; Dutta, P.; Kim, M. J. Chemically Modified Solid State Nanopores for High Throughput Nanoparticle Separation. *J. Phys.: Condens. Matter* **2010**, *22*, 454107–454115.
28. Saleh, O. A.; Sohn, L. L. Quantitative Sensing of Nanoscale Colloids Using a Microchip Coulter Counter. *Rev. Sci. Instrum.* **2001**, *72*, 4449–4451.
29. Sun, L.; Crooks, R. M. Single Carbon Nanotube Membranes: A Well-Defined Model for Studying Mass Transport through Nanoporous Materials. *J. Am. Chem. Soc.* **2000**, *122*, 12340–12345.
30. Ito, T.; Sun, L.; Crooks, R. M. Simultaneous Determination of the Size and Surface Charge of Individual Nanoparticles Using a Carbon Nanotube-Based Coulter Counter. *Anal. Chem.* **2003**, *75*, 2399–2406.
31. Ito, T.; Sun, L.; Bevan, M. A.; Crooks, R. M. Comparison of Nanoparticle Size and Electrophoretic Mobility Measurements Using a Carbon-Nanotube-Based Coulter Counter, Dynamic Light Scattering, Transmission Electron Microscopy, and Phase Analysis Light Scattering. *Langmuir* **2004**, *20*, 6940–6945.
32. Petrossian, L.; Wilk, S. J.; Joshi, P.; Goodnick, S. M.; Thornton, T. J. Demonstration of Coulter Counting through a Cylindrical Solid State Nanopore. *J, Phys: Conf. Series* **2008**, *109*, 012028–012031.
33. Abramoff, M. D.; Magelhaes, P. J.; Ram, S. J. Image Processing with ImageJ. *Biophoton. Int.* **2004**, *11*, 36–42.
34. Hall, J. E. Access Resistance of a Small Circular Pore. *J. Gen. Phys.* **1975**, *66*, 531–532.
35. Gregg, E. C.; Steidley, K. D. Electrical Counting and Sizing of Mammalian Cells in Suspension. *Biophys. J.* **1965**, *5*, 393–405.
36. Wanunu, M.; Sutin, J.; McNally, B.; Chow, A.; Meller, A. DNA Traslocation Governed by Interactions with Solid-State Nanpores. *Biophy. J.* **2008**, *95*, 4716–4725.
37. Wei, R.; Pedone, D.; Zürner, A.; Döblinger, M.; Rant, U. Fabrication of Metallized Nanopores in Silicon Nitride Membranes for Single-Molecule Sensing. *Small* **2010**, *6*, 1406–1414.
38. Bousse, L.; Mostarshed, S. The Zeta Potential of Silicon Nitride Thin Films. *J. Electroanal. Chem.* **1991**, *302*, 269–274.
39. Schoch, R. B.; Han, J.; Renaud, P. Transport Phenomena in Nanofluidics. *Rev. Mod. Phys.* **2008**, *80*, 839–883.
40. Firnkes, M.; Pedone, D.; Knezevic, J.; Döblinger, M.; Rant, U. Electrically Facilitated Translocation of Proteins through Silicon Nitride Nanopores: Conjoint and Competitive Action of Diffusion, Electrophoresis, and Electroosmosis. *NanoLett.* **2010**, *10*, 2162–2167.
41. Yusko, E. C.; An, R.; Mayer, M. Electroosmotic Flow Can Generate Ion Current Rectification in Nano- and Micropores. *ACS Nano* **2010**, *4*, 477–487.
42. Hall, A. R.; Keegstra, J. M.; Duch, M. C.; Hersam, M. C.; Dekker, C. Translocation of Single-Wall Carbon Nanotubes through Solid-State Nanopores. *Nano Lett.* **2011**, *11*, 2446–2450.
43. Soni, G. V.; Dekker, C. Detection of Nucleosomal Substructures Using Solid-State Nanopores. *Nano Lett.* **2012**, *12*, 3180–3186.
44. Tweedie, M. C. K. Inverse Statistical Variates. *Nature* **1945**, *155*, 453.
45. Wanunu, M.; Morrison, W.; Rabin, Y.; Grosberg, A. Y.; Meller, A. Electrostatic Focusing of Unlabelled DNA into Nanoscale Pores Using a Salt Gradient. *Nat. Nanotechnol.* **2010**, *5*, 160–165.
46. Wong, C. T.; Muthukumar, M. Polymer Capture by Electro-osmotic Flow of Oppositely Charged Nanopores. *J. Chem. Phys.* **2007**, *126*, 164903–164908.
47. Nam, S.-W.; Rooks, M. J.; Kim, K.-B.; Rossnagle, S. M. Ionic Field Effect Transistors with Sub-10 nm Multiple Nanopores. *Nano Lett.* **2009**, *9*, 2044–2048.
48. He, Y.; Tsutsui, M.; Fan, C.; Taniguchi, M.; Kawai, T. Gate Manipulation of DNA Capture into Nanopores. *ACS Nano* **2011**, *10*, 8391–8397.